Avoiding Ambient Air and Light Induced Degradation in High-Efficiency Polymer Solar Cells by the Use of Hydrogen-Doped Zinc Oxide as Electron Extraction Material

Ermioni Polydorou,[1,2] Elias Sakelis,[1,3] Anastasia Soultati,[1,4] Andreas Kaltzoglou,[1] Theodoros A. Papadopoulos,[5] Joe Briscoe,[6] Dimitris Tsikritzis,[7] Mihalis Fakis,[2] Leonidas C. Palilis,[2] Stella Kennou,[7] Panagiotis Argitis,[1] Polycarpos Falaras,[1] Dimitris Davazoglou,[1] Maria Vasilopoulou[1,*]

[1]*Institute of Nanoscience and Nanotechnology, National Center for Scientific Research Demokritos, 15310, Agia Paraskevi, Attiki, Greece*
[2]*Department of Physics, University of Patras, 26504 Patras, Greece*
[3]*University of Athens, Physics Department, Section of Solid State Physics, Panepistimioupolis, 15684 Zografos, Athens, Greece*
[4]*Department of Chemical Engineering, National Technical University of Athens, 15780, Athens, Greece*
[5]*Department of Natural Sciences, University of Chester, Thornton Science Park, CH2 4NU, Chester, U. K.*
[6]*Materials Research Institute, School of Engineering and Materials Science, Queen Mary University of London, U. K.*
[7]*Department of Chemical Engineering, University of Patras, 26500 Patras, Greece*
**email: m.vasilopoulou@inn.demokritos.gr*

Keywords: Zinc oxide, Hydrogen doping, Polymer solar cells, Passivation, Long-term stability, Photostability.

Abstract

Polymer solar cells have undergone rapid development in recent years. Their limited stability to environmental influence and during illumination, however, still remains a major stumbling block to the commercial application of this technology. Several attempts have been made to address the instability issue, mostly concentrated on the insertion of charge transport interlayers in the device stack. Although zinc oxide (ZnO) is one of the most common electron transport materials in those cells, the presence of defects at the surface and grain boundaries significantly affects the efficiency and stability of the working devices. To address these issues, we herein employ hydrogen-doping of the ZnO electron extraction material. It is found that devices based on photoactive layers composed of blends of poly(3-hexylthiophene) (P3HT) with electron acceptors possessing different energy levels, such as [6,6]-phenyl-C_{70}butyric acid methyl ester ($PC_{70}BM$) or indene-C_{60} bisadduct ($IC_{60}BA$) enhanced the photovoltaic performance considerably when using the hydrogen-doped ZnO. In particular, it is observed that the maximum power conversion efficiency (PCE) reaches values of 4.62% and 6.65%, respectively, which are much higher than those of the cells with the pristine ZnO (3.08% and 4.51%). Most significantly, the degradation of non-encapsulated solar cells when exposed to ambient or under prolonged illumination is studied and it is found that devices based on un-doped ZnO showed poor environmental stability and significant photo-degradation while those using hydrogen-doped ZnO interlayers exhibited high long-term ambient stability and maintained nearly 80-90% of their initial PCE values after 40 hours of 1.5 AM illumination. All mechanisms responsible for this enhanced device stability are elucidated and corresponding models are proposed. This work successfully addresses and tackles the device instability problem of polymer solar cells and the key findings pave the way for the upscaling of these and, perhaps, of related devices such as perovskite solar cells.

1. Introduction

Polymer solar cells (PSCs) offer a cost-effective path to harvesting the abundant renewable resource of solar energy [1-4]. To date, PSCs based on interpenetrating networks of low bandgap polymer donors and fullerene acceptors have exhibited power conversion efficiencies (PCEs) exceeding 10% for single-junction [5], and 12% for tandem-junction PSCs consisting of stacks of individual cells with complementary absorption [6]. However, to further advance PSCs to photovoltaic applications, efficient devices exhibiting high environmental stability and photostability under constant illumination are required. Besides the design and synthesis of low-bandgap polymer materials with higher absorption efficiency and charge mobilities [7], interface modification using appropriate charge selective interlayers is essential for improving performance [8, 9]. Zinc oxide (ZnO) is a widely utilized n-type material implemented as electron transport interlayer in PSC devices where its inherent transparency, tunable electronic properties, non-toxicity and low cost can be combined to confer superior device properties [10-13]. In addition, ZnO exhibits the advantage of relatively ease thin-film preparation which may be achieved by a diverse range of solution-processing techniques thus being compatible with large area manufacturing [14-17]. However, defects such as oxygen vacancies (V_O) and zinc interstitials (Zn_i) are always present at surface and grain boundaries of ZnO and act as charge traps leading to high recombination rates of the photogenerated charges thus causing significant degradation on the solar cell performance [18-24]. Another well-known feature of ZnO defect states is their sensitivity to several adsorbates like oxygen species, which are always present in air-processed ZnO films and have a negative impact on the photostability of the resulting solar cell [25-27].

A number of endeavors have been directed to solve these issues, and the photovoltaic performance of PSCs using ZnO interlayers has significantly improved in recent years; an example is subjecting the devices to ultraviolet (UV) light exposure, the so-called "light-soaking" approach [28-31], which, however, may have a negative impact on the device lifetime. Also, employing self-assembled monolayers (SAMs), small molecules or high-molar-mass polymers such as poly(ethylene oxide) (PEO) and poly(ethylene glycol) (PEG) on top of ZnO layers can avoid direct contact with photoactive layers, and may also result in the passivation of surface defects [32-40]. However, most of these methods, while reducing the amount of surface defect states, do not passivate the defects present in the grain boundaries of the interlayer. Neither do they improve the intrinsic electrical properties of ZnO films, which are generally not of adequate conductivity as required for efficient electron transport and scale-up of the obtained efficiencies in PSC devices. The conductivity enhancement of the material has been observed under the presence of dopants which also passivate defect states and hamper the adsorption of oxygen. Doping of ZnO electron transport interlayers has been carried out with a variety of different elements, such as aluminum (Al) [41,42], indium (In) [43], cesium (Cs) [44], yttrium (Y) [45], and nitrogen (N) [46], predominantly to improve the conductivity, allowing for the use of thicker interlayers which may be produced in fast production techniques such as roll-to-roll processing. Development of doped charge transport interlayers has been identified to be of paramount importance in achieving highly efficient devices with adequate stability [47,48]. Doping with hydrogen (H) is also expected to simultaneously passivate native defects and favorably affect the n-type conductivity of ZnO; according to the research of Van der Walle, hydrogen forms multicenter bonds with neighboring atoms thus modifying the electronic structure of ZnO for a conductivity boost [49-51]. Recently, our group and others introduced the beneficial surface modification of ZnO by using a hydrogen plasma treatment for efficient inverted PSCs [52,53]. However, simple surface modification cannot afford solar cells with prolonged lifetime and photostabilities since defects present at grain boundaries may be detrimental for the device stability. Here we present an approach to simultaneously modify and thereby stabilize the ZnO surface and bulk *via* hydrogen doping achieved by a simple post-annealing step in hydrogen environment instead of air annealing. Doping of ZnO *via* hydrogen annealing has previously been shown to passivate defects and improve the electrical and optical properties of ZnO [49, 54]. However, the benefits of such doping have not yet been demonstrated in polymer solar cell technology. Here, inverted devices based on photoactive blends of poly(3-hexylthiophene) (P3HT) with either [6,6]-phenyl-C_{70}butyric acid methyl ester ($PC_{70}BM$) or indene-C_{60} bisadduct ($IC_{60}BA$) substantially enhance their photovoltaic performance reaching PCE values of 4.62% and 6.65%, respectively, when using the hydrogen-doped ZnO interlayers, which are much higher than those of the reference cells with the un-doped ZnO (3.08% and 4.51%, respectively). Most significantly, while non-encapsulated devices based on pristine ZnO showed poor environmental stability and significant photo-degradation, those using hydrogen-doped ZnO interlayers exhibited high long-term ambient stability and photostability. In particular, they maintained nearly 80-90% of their initial PCE values after 40 hours of 1.5 AM illumination which represents one of the few cases where high efficiency polymer solar cells exhibit such remarkable photostability [55]. In order to explain in details the differences between devices using un-doped and hydrogen-doped ZnO materials, in addition to the analysis of ambipolar and unipolar devices, we use atomic force microscopy (AFM), scanning electron microscopy (SEM), X-ray and ultraviolet photoelectron spectroscopy (XPS and UPS respectively), Fourier Transform Infrared (FTIR) and UV/Vis absorption spectroscopy, steady-state and transient photoluminescence (PL) spectroscopy, X-ray diffraction (XRD) and contact angle measurements while also performing theoretical calculations.

2. Results and discussion

2.1 Performance and stability improvement in polymer solar cells with hydrogen-doped ZnO interlayers. The configuration of the inverted polymer solar cells using ZnO electron transport interlayer materials is illustrated in Fig. 1a, where the chemical structures of organic semiconductors used in this study are also shown. The cross-section scanning electron microscopy (SEM) image of the inverted device is also shown in Fig. 1a. ZnO films were prepared using a zinc acetate precursor as described in details in the experimental section and then annealed either in air or in hydrogen environment for 20 minutes at temperatures ranging between 100 and 350 ^{o}C. Fig. S1 (shown in Supporting Information) demonstrates the current density-

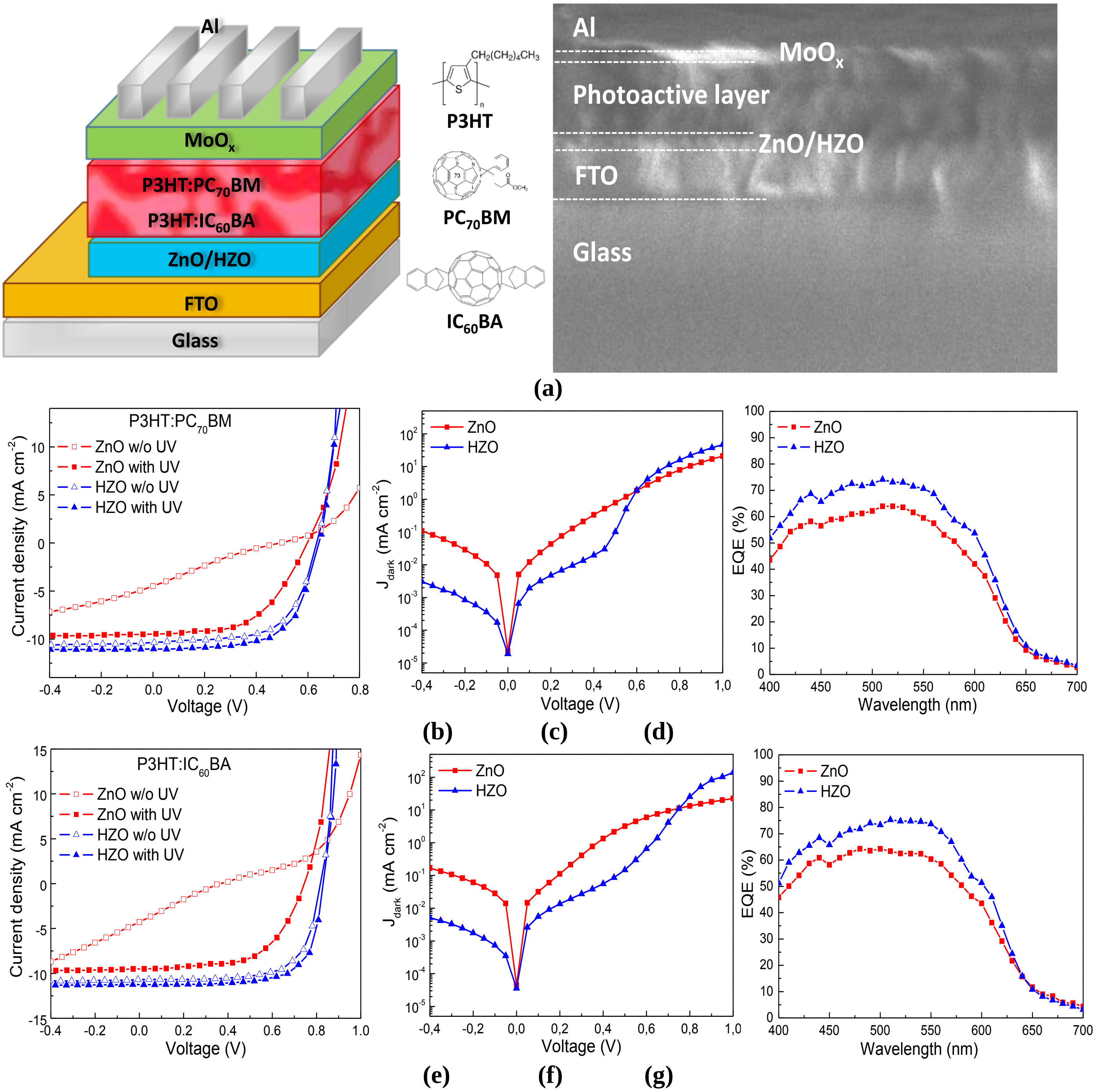

Figure 1 (a) The inverted device architecture and the chemical structures of the organic semiconductors used in this study. SEM image for the cross-section of the inverted polymer solar cell architecture used here: glass/FTO/ZnO or HZO/photoactive layer/MoO$_x$/Al. (b) Current density versus voltage (J-V) characteristics of the P3HT:PC$_{70}$BM-based devices using ZnO/HZO as electron transport interlayers upon 1.5 AM illumination without UV spectral components (blocking filter) and with full 1.5 AM spectrum. (c) The dark J-V curves and (d) EQE measurements of the P3HT:PC$_{70}$BM-based diodes. (e) J-V characteristics of the P3HT:IC$_{60}$BA based devices using ZnO/HZO interlayers upon 1.5 AM illumination without UV spectral components (blocking filter) and with full 1.5 AM spectrum. (f) The dark J-V curves and (g) EQE measurements of the P3HT:IC$_{60}$BA-based diodes.

voltage (J-V) characteristics of devices based on P3HT:PC$_{70}$BM blends measured under 1.5 AM illumination in air. It is shown that devices using the air-annealed ZnO (termed hereafter as ZnO) require an annealing temperature above 200 ^{o}C with the best efficiencies to be achieved for annealing at 250-300 ^{o}C, which is due to the high decomposition temperature of zinc acetate [23]. On the contrary, devices using the hydrogen-annealed ZnO interlayer (termed hereafter as HZO) always exhibit better performance, with high efficiencies achieved even at 150 ^{o}C. This indicates that our methodology for improving performance of PSCs *via* hydrogen-doping (annealing) of ZnO could also find application in flexible devices where lower annealing temperatures are required. However, given that we obtained better stabilities in P3HT:PC$_{70}$BM-based devices having their ZnO annealed above 200 °C, in the following experiments we set the temperature (of both air and hydrogen annealing) at 300 °C. Figs 1b and 1e represent the J-V characteristics under full 1.5 AM simulated solar illumination (with the UV component) of fresh devices using photoactive blends based on P3HT:PC$_{70}$BM and P3HT:IC$_{60}$BA with ZnO and HZO electron transport layers, respectively. The corresponding electrical output parameters of those devices are summarized in Table 1. The dark J-V measurements are also shown in Figs 1c and 1f while the external quantum efficiency (EQE) characteristics of the same devices are presented in Figs 1d and 1g. For the P3HT:PC$_{70}$BM based device with the HZO layer a high PCE of 4.62 % is obtained representing a nearly 50% improvement in comparison to the PCE value of 3.08 % obtained in the device using the air-annealed ZnO interlayer. Similarly, the reference P3HT:IC$_{60}$BA based device with ZnO exhibits an average PCE of 4.51%, while the HZO device showed a 47% higher PCE reaching the value of 6.65%. From the photovoltaic parameters presented in Table 1 becomes evident that HZO interlayer leads to a simultaneous improvement in the open-circuit voltage (V$_{oc}$), short-circuit current (J$_{sc}$) and fill factor (FF). Next, we also measured the J-V curves for similar ZnO/HZO based PSCs under illumination without the UV light content which was excluded through the application of a UV long-pass filter with a cut-off at 400 nm (Figs 1b and 1e). It is observed that the devices using ZnO interlayers yielded an inflection around the V$_{oc}$ point when they were not subjected to UV activation. This suggests that the UV activation is necessary for the induction of photoconductivity and oxygen desorption in the un-doped ZnO layer and the elimination of the electron extraction barrier as also reported by other groups and may explain the lower photovoltaic performance of our reference devices with ZnO (which were not UV activated) as compared to other works [25,55,56]. On the contrary, there was negligible change in the performance of devices using HZO interlayer under illumination without the UV component. Those devices exhibit no inflection in their J-V curve prior to UV exposure suggesting that the HZO interlayer benefited from an improved conductivity due to hydrogen-doping and a reduced electron extraction barrier due to lowering of its workfunction as is also reported for Al-doped ZnO layers [25]. Note that we used non-UV activated ZnO reference devices in order to make a straight comparison with the HZO based ones. Moreover, we also applied ZnO and HZO interlayers in devices using one of the most efficient donor:acceptor combination the PTB7:PC$_{70}$BM mixture. Our preliminary results shown in Fig. S2 evidenced the beneficial effect of hydrogen-doping of the interlayers since the device using HZO layer delivered a high PCE of 7.67% which represents a 44% improvement in comparison to that of the reference cell with the un-doped ZnO (5.30 %). Note that in the case of PTB7:PC$_{70}$BM-based devices the annealing temperature of both ZnO and HZO layers was set at 200 °C where we obtained the best device performance. However, these are preliminary results and further investigation is carried out.

In addition, the dark J-V characteristics (shown here in semi logarithmic scale) are improved greatly in the case of HZO cells, compared to ZnO ones. The distinctly different regions of the J-V curves for diode operation in the dark are seen only in the case of HZO. Importantly, the reverse saturation current density decreased significantly whereas the turn-on (onset) voltage of the corresponding diodes increased. Furthermore, a distinct exponential current rise is seen above the turn-on region with an increase of the injected current noted and a clear shift of the J-V curve. These results suggest that hydrogen-doping in HZO reduces reverse leakage and shunt current while it also facilitates electron extraction probably due to an increase of the built-in field and/or due to enhanced (n-type) conductivity/mobility. As a result, a highly improved diode rectification ratio is observed in HZO-modified interface based solar cells while the increased built-in field may also promote the extraction of photogenerated carriers. Both reduction of the reverse saturation current and increase of the turn-on voltage contribute to the increase of the V$_{oc}$ of the HZO solar cells. If V$_{oc}$ is expressed according to the Shockley equation:

$$V_{oc} = \frac{nK_B T}{q_e} \ln\left[\frac{J_{ph}}{J_o} + 1\right] \tag{1}$$

and taking into consideration that J_0 is given by the expression:

$$J_o = J_{so} \exp\left[\frac{-(HOMO_D - LUMO_A)}{2nK_B T}\right] \tag{2}$$

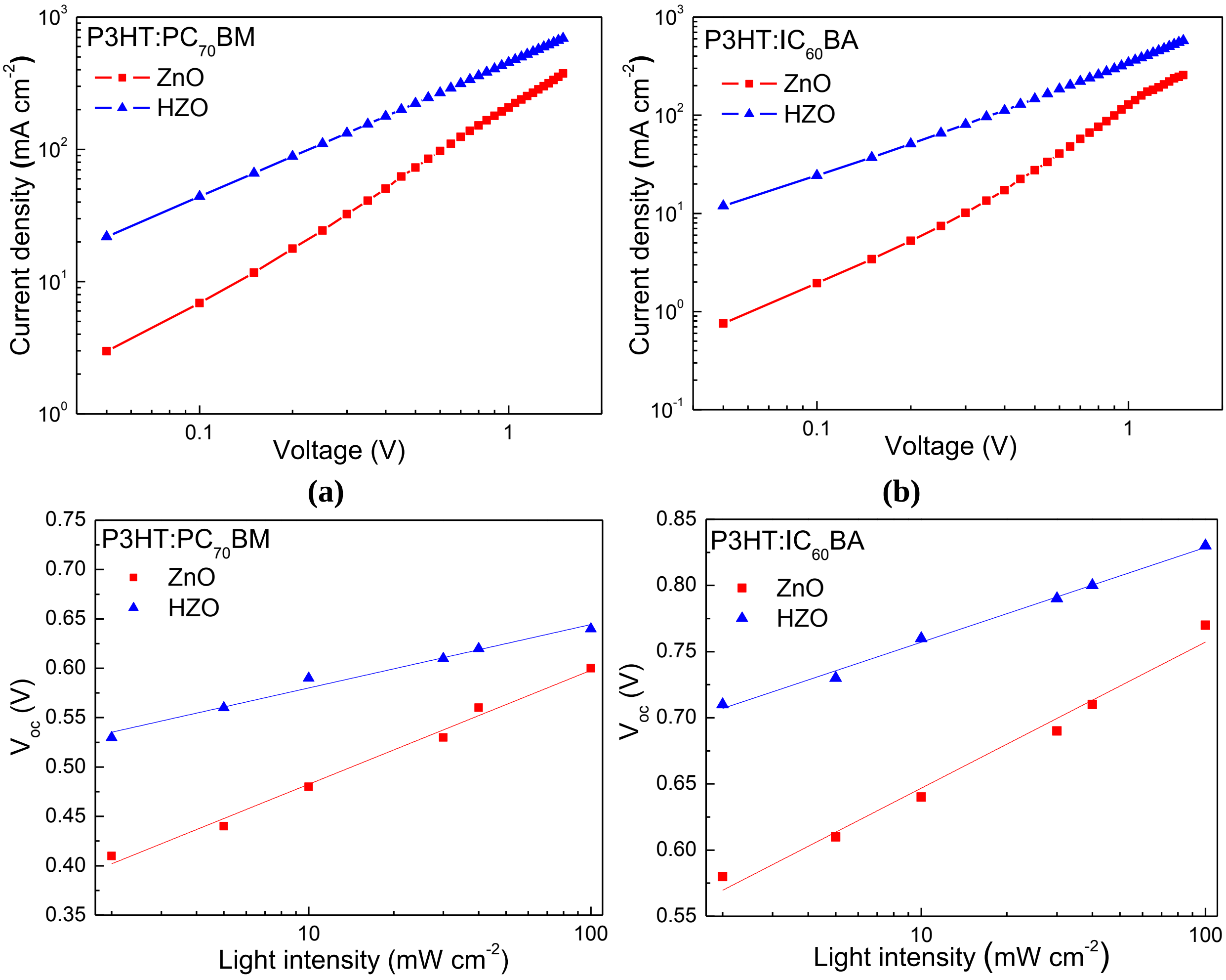

(a) **(b)**

(c) **(d)**

Figure 2 J−V curves in log-log plot obtained in electron-only (a) P3HT:PC$_{70}$BM-based and (b) P3HT:IC$_{60}$BA-based devices with ZnO/HZO interlayers, measured in the dark. Dependence of V_{oc} on light intensity for (c) P3HT:PC$_{70}$BM-based and (d) P3HT:IC$_{60}$BA-based devices with ZnO/HZO interlayers.

then

$$V_{oc} = \frac{nK_B T}{q_e} \ln\left[\frac{J_{sc}}{J_o}\right] + \frac{HOMO_D - LUMO_A}{2q_e} \tag{3}$$

where n is the ideality factor, K_B is the Boltzmann constant, T is the temperature, q_e is the electron charge, HOMO_D is the HOMO of the donor and LUMO_A is the LUMO of the acceptor, J_{sc} is the short-circuit photocurrent density and J_o is the reverse saturation current density. According to (3), a strong decrease of the dark reverse saturation current will result in significant increase of the V_{oc} as in the case of HZO solar cells. In addition, the device with the HZO interlayer exhibits significantly reduced series and larger shunt resistances (Table 1) verifying the overall higher quality of the corresponding diodes and explaining the enhanced short-circuit current (J_{sc}) and fill factor (FF) obtained in the device with the HZO interlayer. The large improvement in J_{sc} is confirmed by the external quantum efficiency (EQE) measurements where HZO cells exhibit an enhanced efficiency throughout the full spectral range. Note that, by integrating the product of the incident photon flux density with the EQE values over the 350 to 750 nm wavelength regime predicted short-circuit photocurrents, J_{sc}^{EQE}, attained by the cells can be calculated (Table 1). The close proximity of the J_{sc} and J_{sc}^{EQE} is an indication for low bimolecular recombination in these devices.

2.2 Additional devices characterization, nanomorphology and photophysical properties of photoactive layers on zinc oxides. The decrease in series resistances of HZO devices indicates that electrons are extracted more efficiently as verified from the J-V characteristics taken in electron-only devices with a structure FTO/ZnO or HZO/P3HT:PC$_{70}$BM/Al (Fig. 2a) or FTO/ZnO or HZO/P3HT:IC$_{60}$BA/Al (Fig. 2b) where the MoO_x/Al hole selective contact is replaced with simple Al, which is able to inject electrons into the

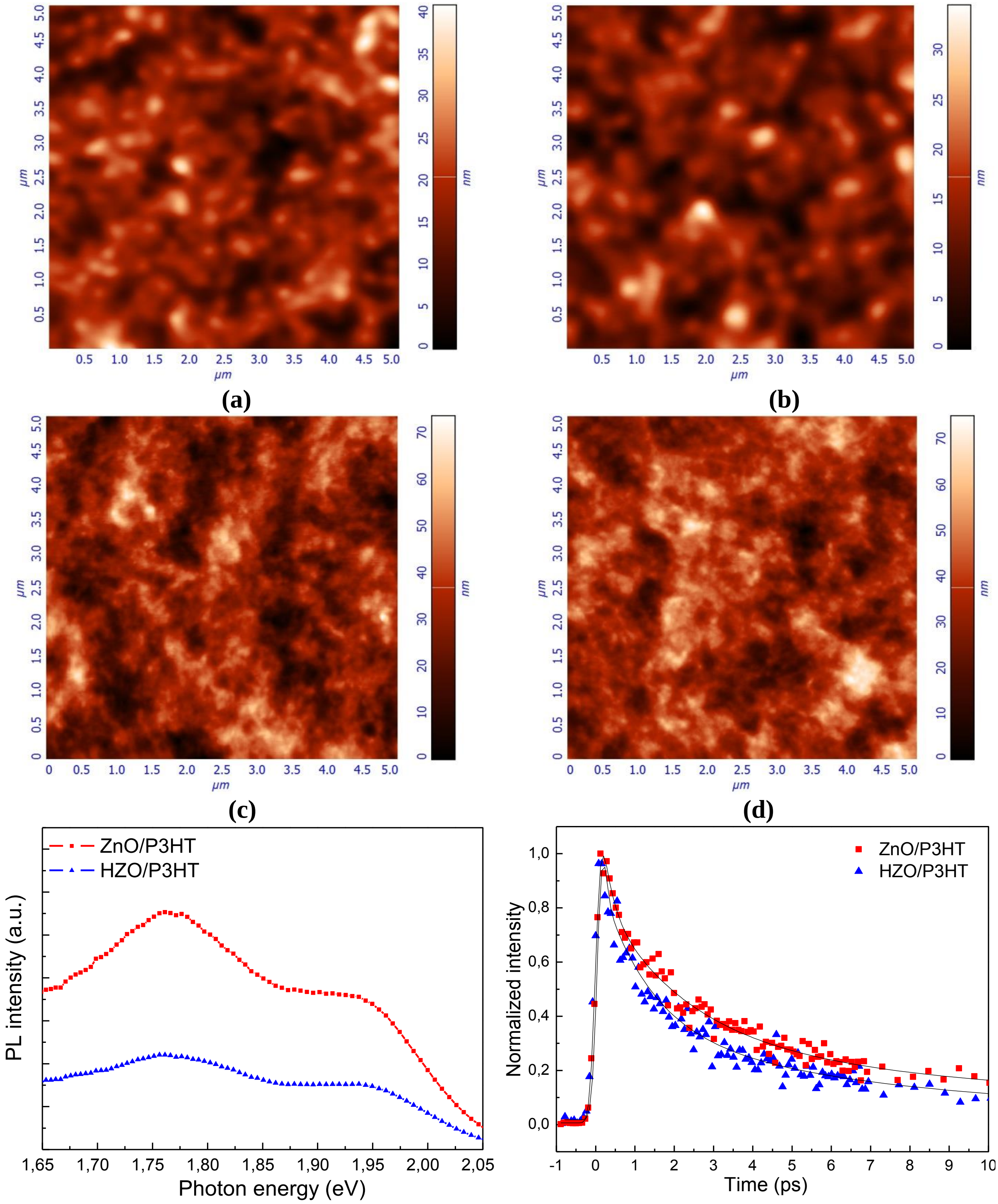

(a) (b) (c) (d) (e) (f)

Figure 3 2D atomic force microscopy (AFM) topographies (5x5 μm) of (a), (b) P3HT:PC$_{70}$BM 120 nm thick films, and of (c), (d) P3HT:IC$_{60}$BA 200 nm thick films deposited on ZnO (a and c) and HZO (b and d) films. (e) Steady-state PL spectra of P3HT on ZnO/HZO layers and (f) Transient PL dynamics of P3HT thin film (10 nm) on different ZnO layers detected at 670 nm.

lowest unoccupied molecular orbital (LUMO) of fullerene acceptors. It is evident that both devices based on ZnO show small current densities in the forward direction while a substantial increase in electron current is found in the HZO-based devices. This clearly corroborates the enhancement of selectivity of the HZO/organic interfaces while the increase in the shunt resistance (Table 1) also suggests that there is less interfacial recombination in the HZO devices. Further evidence for multiple operational recombination channels in the complete solar cell devices based on P3HT donor and different acceptors comes from steady-state J-V measurements where we monitor the variation of V_{oc} of P3HT:PC$_{70}$BM and P3HT:IC$_{60}$BA-based devices under different light intensities (Figs 2c and 2d). We find that both kinds of P3HT-based devices exhibit slopes of V_{oc} versus natural logarithmic of the light intensity larger than KT/q (1.91 KT/q and 1.84 KT/q, respectively) indicating a strong dependence on light intensity when using the ZnO interlayers, which can be assigned to significant surface recombination at ZnO/organic interfaces. In particular, these high slopes seem to imply an increased number of trap states and a, concomitant, large increase in the number of Shockley-Read-Hall (SRH) (monomolecular) or trap assisted recombination processes in the reference cells which is ascribed to an enhanced rate of surface recombination and can be associated with the low selectivity of the cathode contact as surface trap defects dominate recombination [57]. On the contrary, the slopes in the HZO based devices are significantly lower (1.09 and 1.18 KT/q for the P3HT:$PC_{70}BM$ and P3HT:$IC_{60}BA$-based devices, respectively) indicating a slower surface recombination rate and enhancement of selectivity of the cathode contact approaching conditions where bimolecular (e.g. Langevin) recombination dominates. Note that we also verified a similar trend in the slope changes of V_{oc} versus light illumination for the more efficient active system (PTB7:$PC_{70}BM$, Fig. S3) which verifies that changes in the slope can be attributed to different recombination rates at the cathode contact of the devices.

Table 1 Photovoltaic parameters of fresh solar cells having the configuration glass substrate/FTO/ZnO or HZO interlayer /photoactive layer/MoO_x/Al (mean values and standard deviations were extracted from a batch of 36 devices).

	J_{sc} (mA/cm^2)	V_{oc} (V)	FF	PCE (%)	J_{sc}^{EQE} (mA/cm^2)	R_s (Ω cm^2)	R_{sh} (Ω cm^2)
P3HT:$PC_{70}BM$							
ZnO	9.5(±0.15)	0.60(±0.01)	0.54(±0.02)	3.08	9.6	6.1	2100
HZO	11.1(±0.10)	0.64(±0.01)	0.65(±0.01)	4.62	11.2	4.8	7900
P3HT:$IC_{60}BA$							
ZnO	9.6(±0.20)	0.77(±0.01)	0.61(±0.02)	4.51	9.7	6.3	2605
HZO	11.3(±0.20)	0.83(±0.01)	0.71(±0.02)	6.65	11.3	3.3	5650

Because HZO layer was found to exhibit larger and more uniform distribution in topographic grains than ZnO (Fig. S4) as well as different surface energy (as indicated from contact angle measurements shown in Fig. S5), we next studied the differences in surface nanomorphology of the photoactive blends deposited on different ZnO substrates. The AFM topography images are shown in Figs 3a-d. It is observed that the distribution of donor and acceptors and their interpenetrating networks are not very different when deposited on different zinc oxide materials. However, a small reduction in the RMS roughness of the blends deposited on HZO layer is observed (4.6 nm for P3HT:$PC_{70}BM$ and 9.9 for P3HT:$IC_{60}BA$) when compared with blends deposited on ZnO (5.5 nm and 10.6 nm, respectively). This indicates that the film formation and physical contact at the HZO/ photoactive layer interface is more uniform and should lead to a more uniform electrical contact as indicated from the reduced series resistance and increased shunt resistances of HZO solar cells (Table 1). Note that a small reduction in the RMS roughness was also confirmed for 10 nm thin P3HT:$PC_{70}BM$ and P3HT:$IC_{60}BA$ films deposited on HZO layers (Fig. S6) which indicates that hydrogen present on zinc oxide surface may improve photoactive blend nanomorphology, as previously reported by our group [58]. However, the improvement is not sufficient in order to explain the large enhancement in performance of the devices using HZO material.

Hydrogen-doping induced passivation of zinc oxide is the most prevalent hypothesis and was further probed by measuring the photophysical properties of P3HT films on ZnO and HZO layers. Steady state photoluminescence (PL) measurements on thin P3HT (~10 nm) films deposited on ZnO and HZO layers are shown in Fig. 3e. Two emission peaks are observed at 1.95 eV and 1.75 eV corresponding to the 0-0 transition and the 0-1 and 0-2 sidebands. An overall reduction of PL intensity is observed for P3HT deposited on HZO layer, showing increased ability of electron transfer from the photoactive layer to HZO interlayer. This is also confirmed by using transient spectroscopy to observe the excited state dynamics. The transient measurements were performed using the fs up-conversion technique upon excitation at 400 nm and detection at 670 nm (Fig. 3f). Fitting of the PL decays was made through multi-exponential functions and the results are summarized in

Table 2. When P3HT is deposited on ZnO layer the average time-constant is calculated as 3.90 ps, while the HZO layer accelerates the electron decay process, with observed time constant of 1.78 ps. Overall, the steady state and transient PL measurements described here provide significant evidence that HZO layers cause enhanced exciton dissociation at the cathode interface which is considered a key challenge in improving the performance of polymer solar cells that equally affect the active layer. Musselman *et al*. proposes that the surface of the oxide, which is directly adjacent to the P3HT, critically influences charge transfer from the P3HT, and that the slower decay rates obtained with the un-doped ZnO surfaces follow from a larger density of trapped electrons on chemisorbed negatively charged oxygen molecules at the surface, which inhibit exciton dissociation and charge transfer from the P3HT to the oxide [46].

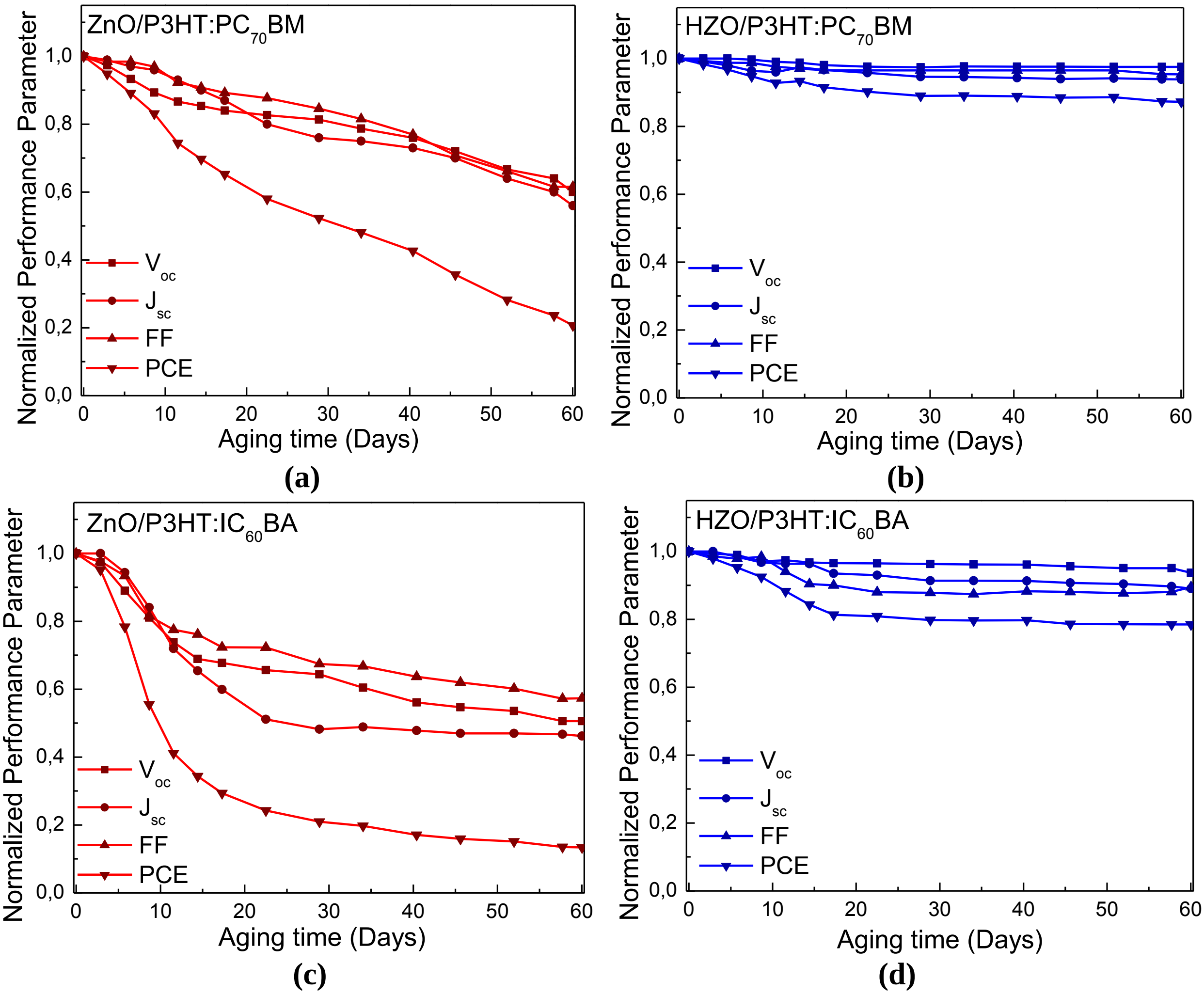

(a) **(b)**

(c) **(d)**

Figure 4 Stability measurements in ambient air: Variation of PCE, J_{sc}, V_{oc} and FF over a period of 60 days for P3HT:PC$_{70}$BM-based devices using (a) ZnO and (b) HZO interlayers and for P3HT:IC$_{60}$BA-based devices using (c) ZnO and (d) HZO interlayers.

Table 2 Fitting parameters, obtained by means of a three-exponential function, of the P3HT films on ZnO substrates with different treatment. Excitation wavelength: 400 nm. Detection wavelength: 670 nm.

Sample	**A_1**	**t_1 (ps)**	**A_2**	**t_2 (ps)**	**A_3**	**t_3 (ps)**	**$\langle t \rangle$ (ps)**
ZnO/P3HT	0.36	0.24	0.44	2.2	0.20	14	3.90
HZO/P3HT	0.47	0.10	0.34	1.2	0.19	7	1.78

2.3 High stability of polymer solar cells with HZO interlayers. In addition to the significant efficiency enhancement, the ambient stability of non-encapsulated devices is also substantially improved when using the HZO layer as shown in Fig. 4 where the variation over aging time of PCE, J_{sc}, V_{oc} and FF for P3HT:$PC_{70}BM$ and P3HT:$IC_{60}BA$ based devices using ZnO (Figs 4a and 4c, respectively) or HZO (Figs 4b and 4d, respectively) interlayers, is shown. It is evident that the operational characteristics of devices using HZO interlayers exhibited high stability preserving 87% of their original PCE values for the P3HT:$PC_{70}BM$ device and 80% for the P3HT:$IC_{60}BA$ after being stored in ambient conditions for 60 days. In contrast, the PCE of P3HT:$PC_{70}BM$ and P3HT:$IC_{60}BA$ devices using air-annealed ZnO interlayers degraded to 20% and 14% of their original values, respectively, when stored under the same conditions. This result proves that hydrogen doping of ZnO can protect the photoactive layer from degradation in air and improve the long-term stability of devices effectively.

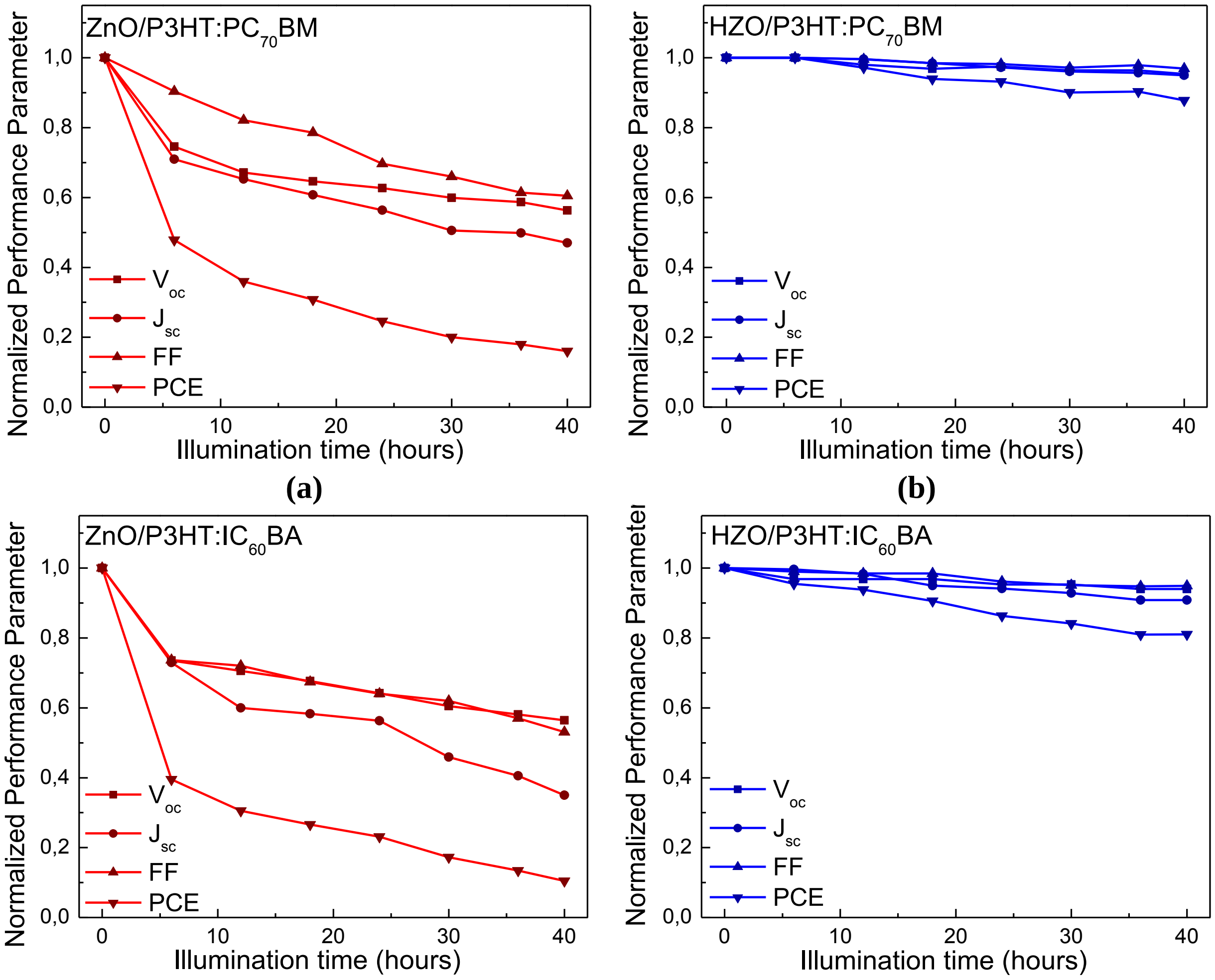

(a) (b)

(c) (d)

Figure 5 Photostability measurements: Variation of PCE, J_{sc}, V_{oc} and FF of degraded under AM1.5G simulated sunlight for 40 h solar cells based on P3HT:$PC_{70}BM$ photoactive blend using (a) ZnO and (b) HZO interlayers and on P3HT:$IC_{60}BA$ photoactive blend using (c) ZnO and (d) HZO interlayers.

Photostability of polymer solar cells also represents a key requirement for the commercialization of this technology. We therefore investigated the degradation of our devices using ZnO or HZO interlayers under constant AM 1.5G illumination in ambient air [59]. As shown in Figs 5a and 5c, after 40 hours of illumination the PCE of P3HT:$PC_{70}BM$ and P3HT:$IC_{60}BA$ devices decreased to 16% and 11% of their original values, respectively, when using the ZnO interlayer, while in the HZO-based devices they maintained 88% and 81% of their values (Figs 5b and 5d). Since the solar cells differ only on the nature of their electron transport interlayers, the differences in their overall photostability can be ascribed to degradation process involving the interlayer. It is reasonable to assume that oxygen adsorption on the ZnO surface during air processing causes the degradation of J_{sc}, V_{oc} and FF under illumination, via formation of shunts by promoting the recombination of holes from the HOMO level of P3HT, as discussed in section 2.5. The small decrease of the operational characteristics of the device using the HZO interlayer could be ascribed to degradation mechanisms common to all devices that equally affect the active layer. Notably, devices using the previously reported by our group hydrogen-plasma treated ZnO (H:ZnO) electron extraction materials [52], they found to maintain only 40-45 % of their original PCE values in both type of PSCs when subjected to constant illumination for 40 hours (Fig. S7). This clearly indicates that simple surface modification cannot afford solar cells with prolonged photostabilities since defects present at grain boundaries may be detrimental for the device stability. The simultaneous modification of ZnO surface and bulk *via* hydrogen-doping proposed here offers a viable route in achieving PSC devices with superior photostability.

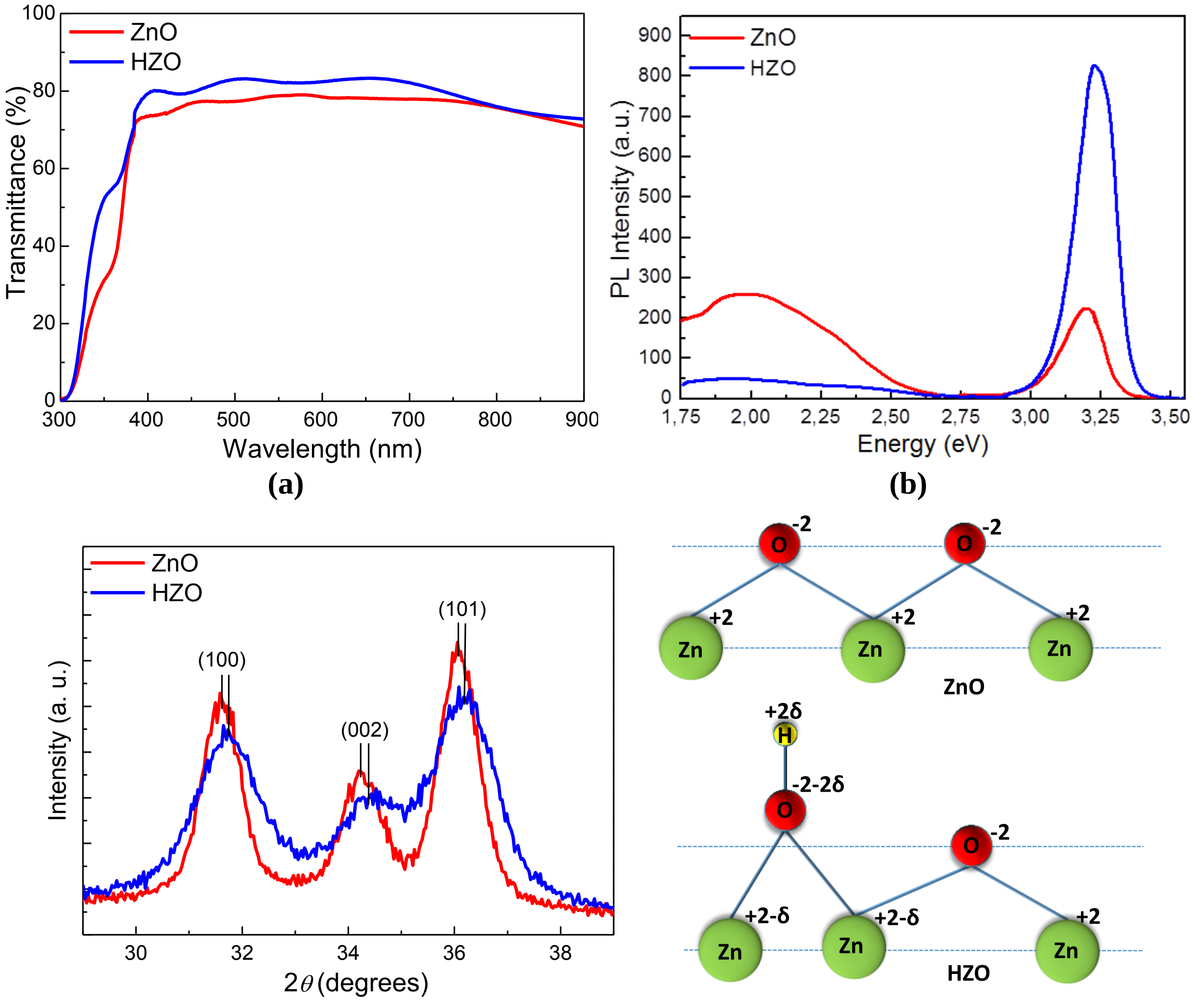

(a)

(b)

(c)

(d)

Figure 6 (a) Transmittance spectra of ZnO and HZO films and (b) steady-state PL spectra of the same films. (c) XRD patterns of ZnO and HZO films. (d) Schematic illustration of charge redistribution due to hydrogen binding to B-site oxygens. This also results in the weaker $Zn_B \cdots O_B$ bonds and consequently, in the $Zn_B \cdots Zn_B$ distances being shorter than the $Zn_A \cdots Zn_A$ distances.

2.4 Optoelectronic properties and nanoscale structure of ZnO and HZO layers. The origin of the improved efficiency and photostability for the devices using the HZO interlayer as compared to pristine ZnO may be ascribed to several reasons including a conductivity boost via hydrogen doping [60]. To investigated hydrogen's contribution to the conductivity of ZnO we performed Hall measurements on samples with a thickness of about 400 nm (obtained by repeating the spin-coating process ten times while films were dried at 90 ^{o}C between subsequent coating steps). Four-point Van Der Pauw Hall measurements revealed a strong reduction in resistivity of the hydrogen-doped sample (from 91.31 Ohm cm for air-annealed ZnO to 0.80 Ohm cm for the HZO film) which was caused from a significant increase in electron mobility (from 0.37 cm^2/Vs for ZnO to 25.34 $cm^2/V\ s$ for HZO) and a moderate increase in carrier concentration (from $1.85x10^{17}\ cm^{-3}$ to $3.08x10^{17}\ cm^{-3}$). In polycrystalline thin films like ZnO, the electron mobility can be limited mainly by the electron scattering within the grains e.g. the scattering by lattice defects or the electron scattering that occurs at the grain boundaries, due to the potential barrier formed at these locations [61]. In the latter case, the electron mobility should increase if the grain size is increased (because of the decrease of the grain boundary density), as was observed in the case of HZO films (Fig. S4). In addition, when hydrogen is incorporated within the film, it passivates lattice defects. The above can explain the significant increase in mobility with consequent decrease in resistivity by almost two orders of magnitude which makes this doped oxide a suitable candidate for use in a broad range of solution based organic and inorganic electronic applications. It is worth noting that, the relatively small increase in carrier concentration of HZO sample implies that this film exhibit no loss of its hole blocking capability which has been previously connected with the increase in carrier concentration [46,59]. In addition, HZO films are highly transparent with the transmittance in the visible region over 84% while the corresponding value for the ZnO films is around 78% (Fig. 6a). Note that the absorption spectra of ZnO/HZO films are very similar resulting in the estimation of same energy gap (E_g=3.3 eV, as derived from tauc plot) for both materials (Fig. S8). In the case of ZnO light absorption at energies below the absorption edge, i.e., within the visible, is induced by transitions between states within the gap and the conduction band. The hydrogenation of the material eliminates these states thus resulting in an increase of transmission [61, 62]. Similar phenomena have been observed in the past in other materials the most striking case being that of amorphous Si, which when un-hydrogenated its band gap is full of states excluding its doping, while when hydrogenated the gap “clears”, the material may be doped in n and p polarities, permitting the formation of electronic devices. This enhancement of transmission is also observed at wavelengths near 900 nm (see Fig. 6a) also facilitates the formation of interference fringes since the light is permitted to oscillate between the two interfaces of the film (with air and substrate) without to be absorbed. This leads to the formation of an additional maximum observed in Fig. 6a. It must be noted at this point, that if the thickness of the film was different a minimum, instead of a maximum, could equally well have been formed.

Hydrogen-doping-induced passivation of defect states present at surface and grain boundaries of ZnO is also expected to make our devices very resistive to the degradation processes due to a reduced amount of adsorbed oxygen molecules inside the interlayer. In this context, photoluminescence (PL) spectroscopy is a useful technique to disclose the density of defects on ZnO and the effect of hydrogen doping on these defects. PL spectra of ZnO and HZO samples, obtained at room temperature with excitation at 325 nm, are shown in Fig. 6b. It is apparent that the spectrum of the air-annealed film is dominated by a broad emission in the visible wavelength region which is attributed to native point defects (V_{Zn}, V_O) of ZnO showing also a smaller band-to-band sharp near-band emission (NBE) peak at 3.27 eV [63]. On the contrary, the spectrum of the HZO film is only governed by the NBE emission which is significantly enhanced due to the suppression of the defect states that are located within the energy gap of ZnO and act as recombination centers. Electrons in defects sites are likely to interact with molecular oxygen from the ambient air during film preparation, leading to the formation of chemisorbed O_2^-species, resulting in severe degradation of ZnO-based devices.

In addition to the above analyses, we performed XRD characterization of the ZnO and HZO films prepared on silicon substrates (zoomed-in patterns in Fig. 6c and full-range patterns in Fig. S9). Both films were indexed as wurtzite ZnO [24]. The diffraction peaks for the hydrogen annealed sample are significantly broader than for the untreated sample, as a result of reduced crystallinity. Moreover, the hexagonal lattice parameters decrease significantly from ZnO ($a = b$ = 3.241(5) Å and c = 5.192(7) Å) to HZO ($a = b$ = 3.226(11) Å, c = 5.160(18) Å), which indicates shorter inter-planar distances in the hydrogen-annealed sample [64, 65]. This can be unambiguously attributed to the intercalation of hydrogen within the HZO oxide’s lattice, as also indicated by Fourier transform infrared (FTIR) spectra shown in Fig. S10. The peaks observed in the 400-650 cm^{-1} region are characteristics of the stretching modes of ZnO [66]. However, in the spectrum of HZO film a significant increase of the broad peak at 3400-3900 cm^{-1}, which consists of absorption lines that are all in the characteristic wavenumber range of the -OH stretch modes, and the appearance of a band at around 1600 cm^{-1}, which can be assigned to the first overtone of fundamental stretching mode of –OH, indicate the presence H atoms bonded to O in the hydrogen annealed sample. The binding of H to O shifts the electron density on oxygen away from the Zn-O-Zn bonds, as illustrated schematically in Fig. 6d. Effectively, this is equivalent to the oxygen on site “B” being less electronegative, and as a result, the Zn-O bond becoming less ionic, with larger electron density residing on the B-site zinc compared to that in the wurtzite structure (site “A”). The less ionic $Zn_B \cdots O_B$ bond results in a longer $Zn_B \cdots O_B$ distance, compared to the $Zn_A \cdots O_A$ bond away from the hydrogen site. This in turn leads to the $Zn_B \cdots Zn_B$ distances being shorter than the $Zn_A \cdots Zn_A$ distances, as estimated from the XRD patterns. In addition, the binding of an H atom to O results in an increase of electronic occupancy in the bottom of the conduction band with simultaneous passivation of inter-gap defect states (mainly arising from O dangling bonds) as the H 1s orbital combines with the O 2p dangling bonds state and results in a fully symmetric bonding state in the valence band, and an antibonding state in the conduction band. The electron that would occupy this antibonding state is then transferred to the conduction-band minimum, making the interstitial hydrogen, H_i, a shallow donor (Fig. S11a). Note that, according to Van der

Walle, substitutional hydrogen is also a shallow donor in ZnO since its electron can be transferred to the bottom of the conduction band via bonding with Zn 4s dangling bonds (Fig. S11b) [49, 50]. Notably, in the XRD pattern of HZO film the intensity of of (002) peak is decreased as compared to those attributed to (100) and (101) planes suggesting that this film has different surface energy (less polar surface) than ZnO, as also indicated by contact angle measurements (Fig. S5). Such a difference in contact angles means that hydrogen treatment results in a less hydrophilic surface that favors the smoother deposition of the organic compounds. In addition, zinc oxide surfaces that contain more polar faces (like air-annealed ZnO) might react with the organic semiconductor disrupting the interface [24], which could also be the origin of the faster degradation of the devices based on ZnO.

2.5 Experimental study (XPS/UPS) and theoretical calculations on the electronic structure of ZnO and HZO layers. Further investigations on constituent elements and the presence of defects at the surface of the samples have been performed using XPS spectroscopy. The representative XPS Zn 2p peaks of air and hydrogen-annealed samples are shown in Fig. S12. Zn $2p_{3/2}$ and Zn $2p_{1/2}$ core level spectral lines appear highly symmetric and their binding energy positions are identical in both films. Both films display a doublet at 1021.6 eV and 1044.8 eV corresponding to the Zn $2p_{3/2}$ and $2p_{1/2}$ core levels of stoichiometric ZnO [67]. Figs 7a and 7b show the XPS O1s peaks of ZnO and HZO films. The peaks appear to be asymmetric, indicating the presence of more than one oxygen species in the surface of those films. The deconvoluted O1s peak has two main components at the binding energy positions of 530.4, and 532.0 eV. The low binding energy component corresponds to the O^{2-} state of lattice oxygen (Zn–O) whereas the high binding energy component is attributed to adsorbed OH/H_2O or other surface oxygen species at the films surface as well as to oxygen vacancies (V_O) [68, 69]. The contribution of the high binding energy component is smaller in the HZO film which may indicates that hydrogen annealing reduces oxygen vacancies since FTIR study clearly evidenced that -OH species are increased in the HZO film. Reduced density of oxygen vacancies results in removal of chemisorbed oxygen promoting the improvement of device performance and overall stability.

In addition, UPS spectroscopy was used to experimentally probe the electronic structure of the valence band of ZnO and HZO layers on FTO substrates. Since these samples were prepared ex-situ in order to eliminate the surface contamination before introducing to ultra-high vacuum they were transferred into argon filled vials. The UPS spectrum of ZnO film (Fig. 7c) shows two distinct peaks at ~5.0 eV and ~11.0 eV binding energies which arise from the O 2p and Zn 3d bands, respectively. For the ZnO film a work function (W_F) of 4.1 eV is determined, while HZO shows a reduced W_F of 3.9 eV. The W_F shift towards lower values of the HZO sample can be explained as follows: During hydrogen annealing of ZnO -OH groups are formed on its surface (as well as its bulk) as discussed above. Hydroxyl is however electrically polar, with a dipole moment of 1.67 Debye (5.57x 10^{-30} Cm) [70]. It is thus reasonable to assume that the formation of hydroxyl groups on the surface of HZO sample would readily lead to the formation of an electrical dipole which consequently reduces about 0.2 eV the surface work function of the sample. The reduction in work function between ZnO and HZO is expected to increase the built-in voltage across the organic bulk in the photodiode, improving the electron extraction properties of the cathode, and thus increasing the V_{oc} of the device as observed above. The energy level alignment of various layers used in our devices considering vacuum level alignment (before contact) is illustrated in Fig. 7d demonstrating that the W_F of HZO nearly aligns with the LUMO level of $PC_{70}BM$ while also locates closer to the LUMO of $IC_{60}BA$ as compared to ZnO thus facilitating electron extraction (the energy levels of organic materials were taken from the literature [71], while the W_F of MoO_x was previously measured by our group [72]). Since the reported W_F values and the associated negative integer charge transfer states of e.g. $PC_{70}BM$ are within the range of 4.3-4.6 eV [73], a negative interfacial dipole (with its negative pole towards$PC_{70}BM$) is also expected to be formed at the zinc oxide/$PC_{70}BM$ interface as both substrates' work function is smaller than that of the organic. Such negative dipole, which is larger in the case of HZO material, is beneficial for the device performance as the associated built-in dipole field may further assist electron transfer. Overall, the application of hydrogen-doping greatly enhances the electron selectivity of zinc oxide material. Note that, when both types of electron transport layers have been placed under 1 hour of 100 mW/cm^2 full 1.5 AM illumination in air, we found that their W_F increased to 4.3eV (Fig. S13). This is in agreement with previous studies demonstrating that for UV-light soaking of ZnO in the presence of oxygen, the work function increases which was attributed to a decrease of the oxygen-defect component of the ZnO caused by oxygen atom vacancy filling occurring mainly at the surface of the ZnO films as a result of oxygen readsoprtion [74]. On the contrary, hydrogen-doping studied here induces a decrease in work function and surface-desorption of chemisorbed oxygen resulting in effective passivation of defect states *via* the formation of hydroxyl group.

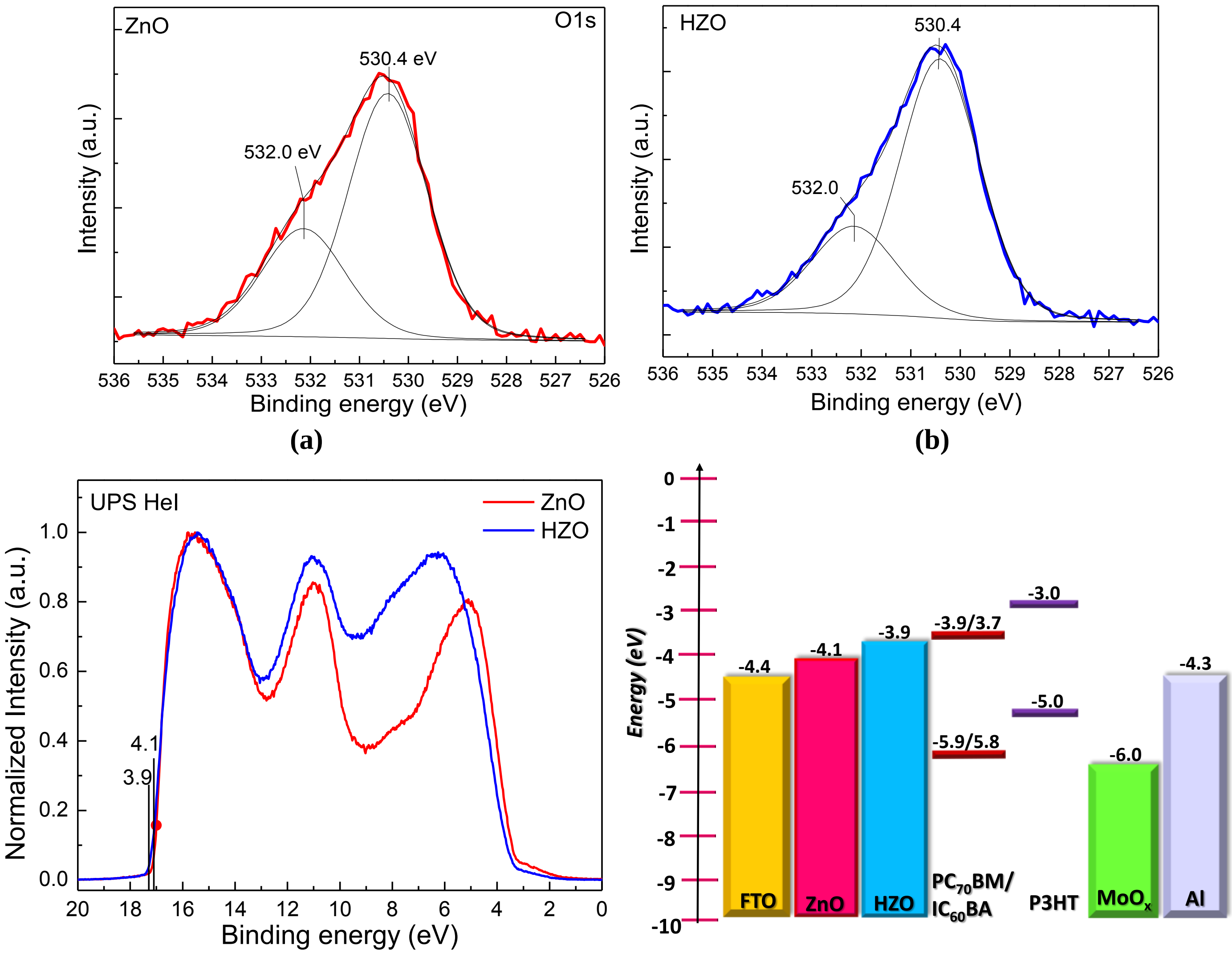

(a) **(b)**

(c) **(d)**

Figure 7 XPS O 1s peaks of (a) ZnO and (b) HZO samples. (c) UPS spectra taken on the ZnO and HZO films deposited on an FTO substrate. (d) Schematic energy level diagram of various layers used in the device structure considering energy level alignment (before contact).

To further support our argument that passivation of oxygen vacancies might be the main reason for enhanced performance and stability of PSCs we also carried out Density Functional Theory (DFT) calculations. We focus at the O-terminated ZnO(0002) surface (Fig. S14a), hereafter mentioned simply as the ZnO surface, which has the lowest surface energy in the O- and H-rich limits [75]. The density of states (DOS) of the ZnO surface is plotted in Fig. 8a. We observe that states located 0.1 eV below the valence band maximum mainly consist of O 2*p* levels with nearly no contribution from Zn states. We also observe the appearance of sharp states located at -1.4, -1.1, -0.7 and 0.2 eV (Fig. 8a and S14c), which are related mostly to surface oxygen *p* and hybridized *d* orbitals. This provides proof of our hypothesis that surface oxygen unsaturated bonds are mainly responsible for trap states appearing at the bottom of the ZnO conduction band. Next, the ZnO(0002) slab was optimized after all surface oxygen orbitals were saturated via bonding with hydrogen atoms to form hydroxyl groups (Fig. S14b). The coverage density of hydrogen was calculated to be $\rho = 10.93 \cdot 10^{14}$ cm^{-2} and the energy released during the formation of each hydroxyl group was found to be -3.72 eV, showing that this process is energetically favorable. In order to examine the effect of hydrogen doping on the surface electronic structure, we plot the density of states after having introduced (i) interstitial hydrogen atoms bonded to surface oxygen forming hydroxyl groups, and (ii) a hydrogen substitutional defect, replacing an oxygen vacancy, following previous work by Janotti *et al.* [51]. (Fig. 8b). We observe that when hydrogen doping occurs, there is a considerable suppression of the unsaturated surface oxygen states. Surface hydrogen doping provides for electron transfer from hydrogen to oxygen atoms, reducing the electronegativity of the latter. This is confirmed via Bader charge analysis performed on the ZnO slab before and after hydrogen doping, which shows that the formation of surface hydroxyl groups results in charge transfer of 1.08±0.08 electrons, on average, to surface oxygen atoms. At the same time the Zn-O bond becomes less ionic, which in turn results in higher Zn 3*d* and 4*s*-orbital occupancies, and consequently more metallic behavior. Similar results were obtained when hydrogen doping of bulk ZnO occurs (Fig. S15). Taking into account all the above results, we conclude that hydrogen doping occurring during hydrogen annealing of ZnO is responsible for the enhanced performance and exceptional stability of our devices which is in agreement with our hypothesis.

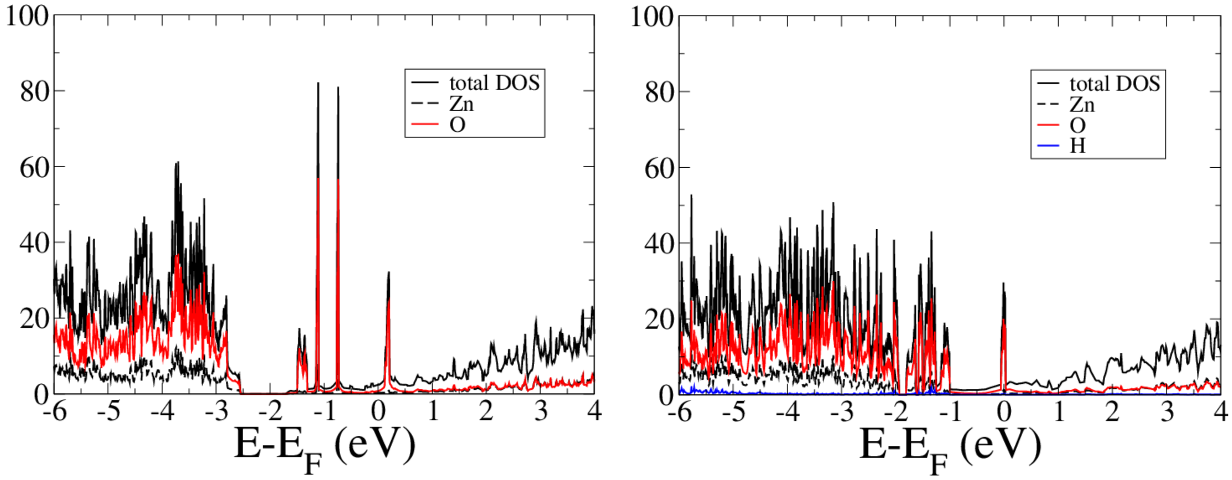

(a) **(b)**

Figure 8 (a) The density of states of the ZnO(0002) surface; (b) The density of states of the ZnO(0002) surface after interstitial hydrogen atoms bonded to surface unsaturated oxygen atoms, with the coverage density of hydrogen calculated to be $\rho = 13.66 \cdot 10^{14}$ cm^{-2} including a substitutional hydrogen defect (Fig. 14b). The total DOS is plotted in solid black line, along with the partial DOS for zinc atoms (black dashed line), oxygen atoms (red solid line), and hydrogen atoms (blue solid line). The Fermi level is set to 0 eV.

3. Conclusions

To summarize, the effectiveness of hydrogen-doping of ZnO on the performance and stability of polymer solar cells has been investigated. It was revealed that simple hydrogen-annealing of ZnO (instead of air-annealing) significantly boosts the efficiency while simultaneously strengthens the stability of the cell. Stemming from synergistic effects, the hydrogen-annealed sample offers several advantages over its air-annealed counterpart including less density of surface traps and defects at grain boundaries followed by removal of chemisorbed oxygen species, more efficient charge separation, reduced electron extraction barrier and better transport capability due to improved conductivity. The combined effects resulted in a remarkable enhancement of V_{oc}, J_{sc} and FF in HZO based PSCs, irrespective of the acceptor used in combination with P3HT as polymer donor in the photoactive blend. Preliminary results taken on PTB7:$PC_{70}BM$-based devices indicated the universality of our approach. In addition, removal of chemisorbed oxygen following the passivation of defect states is suggested to explain the substantial improvement of the stability of the resulting devices when exposed to ambient or are under prolonged illumination. Based on our results, we believe that our prescription of gaining control on the properties of ZnO interlayers based on the interplay of electron donor capability of intercalated hydrogen and induced surface defect passivation constitutes a step forward towards not only efficient PSCs, but also any type of ZnO-based applications.

4. Experimental section

Preparation of ZnO and HZO layers. Solution-processed ZnO films were prepared following a sol-gel method using zinc acetate in 2-methoxyethanol:2-amino-ethanol as a precursor solution [76]. The solution with a concentration of 0.50 M was filtered by a 0.45 μm pore size nylon membrane and then spin-coated at 3000 rpm. Zinc acetate was purchased from Sigma–Aldrich and used without further purification. The ZnO films were then annealed either in air or in pure hydrogen environment for 20 min. Hydrogen annealing was made in a furnace equipped with a quartz chamber, a temperature control system, a vacuum and a gas line. Samples were positioned in the chamber on a graphite susceptor, which heated with the aid of three tungsten lamps of 1000 W each. The temperature of the susceptor (and of the samples on it) was controlled with an automatic temperature control system, which was receiving feedback from a thermocouple positioned in a hole on the graphite and was controlling the power of the lamps. After loading the samples, the chamber was evacuated down to 2 10^{-2} Torr. Then a nitrogen stream was allowed to flow throw it to maintain a pressure of 0.1 Torr and the temperature was raised to the desired point (100-350 °C). After the pre-set temperature was reached, the chamber was evacuated again down to 2 10^{-2} Torr and the hydrogen was introduced in it at a pressure of 1 Torr. At the end of the annealing the chamber was evacuated from hydrogen, nitrogen was introduced, the heating lamps were turn off and the samples were left to cool down to 70 °C under 0.1 Torr of nitrogen.

Device Fabrication. Inverted polymer solar cells were fabricated on fluorinated tin oxide (FTO) coated glass which were purchased from Sigma-Aldrich and served as the cathode electrode. Substrates were ultrasonically cleaned with a standard solvent regiment (15 min each in detergent, acetone, isopropanol and de-ionized water). The ZnO layer (with a thickness of 40 nm) was then deposited followed by appropriate annealing and deposition of the photoactive layer. The active layer consisted of P3HT:$PC_{70}BM$ blend (10 mg ml^{-1} for P3HT, 8 mg ml^{-1} for $PC_{70}BM$ in 1,2 dichlorobenzene) with a thickness of 150 nm or P3HT:$IC_{60}BA$ (17 mg ml^{-1} for P3HT, 17 mg ml^{-1} for $IC_{60}BA$ in 1,2-dichlorobenzene) with a thickness of 200 nm. After spin coating (at 600 rpm for 40 s for P3HT:$PC_{70}BM$ and at 800 rpm for 30 s for P3HT:$IC_{60}BA$) the photoactive layers were left to dry for about 30 min and then annealed at 150 °C for 10 min. PTB7:$PC_{70}BM$ was deposited via spin coating at 1000 rpm for 90 s from solutions with concentration 10 mg ml^{-1} for PTB7, 15 mg ml^{-1} for $PC_{70}BM$ in 1,2 dichlorobenzene where 3% per volume of DIO was added to deliver a thickness of 85 nm and then was left to dry without being subjected to any post-deposition annealing. Note that all depositions and thermal annealing treatments of P3HT:$IC_{60}BA$ and PTB7:$PC_{70}BM$ films were carried out in the inert environment of an argon filled glove-box with oxygen and humidity levels below 1.0 ppm. Then, an approximately 30 nm thick under-stoichiometric molybdenum oxide (MoO_x) layer was deposited on top of the photoactive layer to serve as the hole extraction layer [77]. The devices were completed with a 150 nm thick aluminium anode, deposited in a dedicated thermal evaporator at a pressure of 10^{-6} Torr through a shadow-mask, which defined the device active area to be equal to 12.56 mm^2. The devices were then measured in air at room temperature without additional encapsulation. All chemicals were purchased from Sigma-Aldrich and used with no further purification.

Measurements and Instrumentation. X-ray photoelectron spectra (XPS) and Ultraviolet Photoelectron Spectra (UPS) were recorded by Leybold EA-11 electron analyzer operating in constant energy mode at pass energy of 100 eV and at a constant retard ratio of 4 eV for XPS and UPS respectively. All binding energies were referred to the C 1s peak at 284.8 eV of surface adventitious carbon, respectively. The X-ray source for all measurements was a nonmonochromatized Al Kα line at 1486.6 eV (12 keV with 20 mA anode current). The valence band spectra of Zn oxides were evaluated after recording the UPS spectra of about 400 nm thick films deposited on an FTO substrate. For the UPS measurements, the He I (21.22 eV) excitation line was used. A negative bias of 12.22 V was applied to the samples during UPS measurements in order to separate secondary electrons originating from sample and spectrometer and to estimate the absolute work function value from the high BE cut-off region of the UPS spectra. The analyzer resolution is determined from the width of the Au Fermi edge to be 0.16 eV. The electrical resistivity, Hall mobility and free carrier concentration were determined by Hall-effect measurements at room temperatures in Van der Pauw geometry using a constant magnetic field of 0.5 T. The steady state photoluminescence spectra of P3HT on various substrates were taken by means of a Fluoromax spectrometer (Horiba) upon excitation at 550 nm. The films were placed on a specific holder for solid samples and the spectra were corrected for the sensitivity of the detector. The PL dynamics of the samples were studied under magic angle conditions, by using a femtosecond upconversion technique. The excitation of the samples was realized by means of the second harmonic of a Ti:Sapphire laser at 400 nm. The average power was less than 3 mW while the repetition frequency was 80 MHz. The PL of the samples was collected and focused together with the remaining fundamental fs laser beam on a 0.5 mm BBO crystal to produce frequency mixing. The upconverted beam passed through an iris, filters and a monochromator and was detected by a photomultiplier. The Instrument's Response Function (IRF) was approximately 150 fs. A three-exponential function convoluted with the IRF was used for fitting the dynamics. EQE measurements were carried out using an Autolab PGSTAT-30 potentiostat, with a 300 W Xe lamp in combination with an Oriel 1/8 monochromator for dispersing the light in an area of 0.5 cm^2. A Thorlabs silicon photodiode was used for the calibration of the spectra. All measurements were performed in air. X-ray diffraction (XRD) structural analysis was performed using a Siemens D500 diffractometer with Cu-K*a* radiation. Absorption measurements were taken using a Perkin Elmer Lamda 40 UV/Vis spectrophotometer. FTIR transmission spectra of ZnO films were obtained on a Bruker Tensor 27 spectrometer (at 4 cm^{-1} resolution, 64 scans) with a DTGS detector. The thicknesses of films were measured with an Ambios XP-2 profilometer and a M2000 Woolam ellipsometer. Current density-voltage characteristics of the fabricated solar cells were measured with a Keithley 2400 source-measure unit. Cells were illuminated with a Xe lamp and an AM 1.5G filter to simulate solar light illumination conditions with an intensity of 100 mW/cm^2 (1 sun), as was recorded with a calibrated silicon photodiode. To accurately define the active area of all devices we used aperture masks during the measurements with their area equal to those of the Al contacts (12.56 mm^2).

Computational part. All theoretical calculations were carried out using the Vienna Ab Initio Simulation Package (VASP). Plane-wave basis sets and the Perdew-Burke-Ernzerhof (PBE) gradient-corrected exchange-correlation functional was used throughout the computational part. We incorporated an effective Hubbard U parameter equal to 8.5 eV as implemented and tested by Li et al [78]. All calculations were performed via the projector augmented wave (PAW) method with a plane-wave cut-off energy of 400 eV and a Γ centered k-point grid of 4×4×4 for the bulk and 8×8×1 for the surface calculations. The tetrahedron method with Blöchl corrections of a width of 0.2 eV was used to determine how partial occupancies are set for each wave function. The ZnO surface slab was constructed after PBE+U ion optimization, excluding volume, was performed on bulk ZnO at its crystallographic coordinates; these were taken from work done by Kisi et al [79]. An orthorhombic unit cell was used of dimensions a = 6.50 Å, b = 5.63 Å and c = 5.21 Å, including 8 Zn and 8 O atoms. The ZnO (0002) surface, which is the most stable and exposed crystal surface of ZnO [75], was modeled using 20 Zn and 24 O atoms within an orthorhombic cell of dimensions a = 6.50 Å, b = 5.63 Å and c = 40 Å. All surface cells were separated by a vacuum space of ~30 Å along z-axis. Geometry optimization, with maximum atomic forces of 0.01 e $Å^{-1}$ was carried out for the top two ZnO layers emulating surface relaxation, while the bottom three layers were kept fixed at their crystallographic coordinates representing "bulk" ZnO.

Acknowledgements

This work was performed in the framework of "YDISE" project within GSRT's KRIPIS action, funded by Greece and the European Regional Development Fund of the European Union under NSRF 2007–2013 and the Regional Operational Program of Attica. TP acknowledges use of Hartree Centre computational resources via the 3rd BlueJoule Access Programme, under project No. HCBG125, funded by the U.K. Science and Technology Facility Council (STFC).

Supporting Information

Additional Figures are included in the Supporting Information: J-V characteristics of polymer solar cells based on ZnO electron transport layers processed under different annealing conditions, J-V characteristics and plots of V_{oc} versus light intensity of PTB7:$PC_{70}BM$, AFM topographies and contact angle measurements of ZnO and HZO layers, thin and thick photoactive films nanomorphology, UV-vis absorption spectra of different ZnO layers, XRD patterns and FTIR measurements of ZnO and HZO layers, energy band diagrams, Zn 2p XPS peaks of ZnO and HZO layers, UPS spectra of ZnO/HZO layers before and after light exposure, DFT calculated density of states.

References

[1] G. Gao, J. C. Hummelen, F. Wudl, A. J. Heeger, Science 270 (1995) 1789-1791.
[2] M. A Green, K. Emery, Y. Hishikawa, W. Warta, E. D. Dunlop, Prog. Phot. Res. Appl. 20 (2013) 12-20.
[3] S. Mathew, A. Yella, P. Gao, R. Humphry-Baker, B. F. E. Curchod, N. Ashari-Astani, I. Tavernelli, U. Rothlisberger, Md. Khaja Nazeeruddin, M. Grätzel, Nat. Chem. 6 (2014) 242-247.
[4] N. K. Noel, S. D. Stranks, A. Abate, C. Wehrenfennig, S. Guarnera, A. Haghighirad, A. Sadhanala, G. E Eperon, S. K. Pathak, M. B Johnston, L. Herz, H. Snaith, Energy Environ. Sci. 7 (2014) 3061-3068.
[5] Z. He, B. Xiao, F. Liu, H. Wu, Y. Yang, S. Xiao, C. Wang, T. P. Russell, Y. Cao., Nature Photon. 9 (2015) 174-17.
[6] Z. Yin, J. Wei, Q. Zheng, Adv. Sci. (2016) 1500362.
[7] Y. Li, Acc. Chem. Res. 45 (2012) 723-733.

[8] H.-L. Yipa, A. K.-Y. Jen, Energy Environ. Sci. 5 (2012) 5994-6011.
[9] C. K. Song, A. C. White, L. Zeng, B. J. Leever, M. D. Clark, J. D. Emery, S. J. Lou, A. Timalsina, L. X. Chen, M. J. Bedzyk, T. J. Marks, ACS Appl. Mater. Interfaces 5 (2013) 9224-9240.
[10] S. Chen, J. R. Manders, S.-W. Tsang, F. So, J. Mater. Chem. 22 (2012) 24202-24212.
[11] J. You, C.-C. Chen, L. Dou, S. Murase, H.-S. Duan, S. Hawks, T. Xu, H. J. Son, L. Yu, G. Li, Y. Yang, Adv. Mater. 24 (2012) 5267-5272.
[12] R. M. Hewlett, M. A. McLachlan, Adv. Mater. 28 (2016) 3893-3921.
[13] S. Trost, T. Becker, K. Zilberberg, A. Behrendt, A. Polywka, R. Heiderhoff, P. Görrn, T. Riedl, Sci. Rep. 5 (2014) 7765.
[14] J. Gilot, M. M. Wienk, R. A. J. Janssen, Appl. Phys. Lett. 90 (2007) 143512.
[15] H. Zhang, T. Stubhan, N. Li, M. Turbiez, G. J. Matt, T. Ameri, C. J. Brabec, J. Mater. Chem. A (2014) 18917-18923.
[16] A. Kohan, G. Ceder, D. Morgan, C. Van de Walle, Phys. Rev. B 61 (2000) 15019.
[17] A. Janotti, C. G. Van de Walle, Phys. Rev. B 76 (2007) 5202.
[18] A. Janotti, C. G. Van de Walle, Appl. Phys. Lett. 87 (2005) 122102-3.
[19] K. H. Tam, C. K. Cheung, Y. H. Leung, A. B. Djurišić, C. C. Ling, C. D. Beling, S. Fung, W. M. Kwok, W. K. Chan, D. L. Phillips, L. Ding, W. K. Ge, J. Phys. Chem. B 110 (2006) 18917-18923.
[20] M. Hartel, S. Chen, B. Swerdlow, H.-Y. Hsu, J. Manders, K. Schanze, F. So, ACS Appl. Mater. Interfaces 5 (2013) 7215-7218.
[21] A. Gadisa, Y. Liu, E. T. Samulski, R. Lopez, Appl. Phys. Lett. 100 (2012) 253903
[22] Y. Jin, J. Wang, B. Sun, J. C. Blakesley, N. C. Greenham, Nano Lett. 8 (2008) 1649-1653.
[23] B. A. MacLeod, B. J. T. de Villers, P. Schulz, P. F. Ndione, H. Kim, A. J. Giordano, K. Zhu, S. R. Marder, S. Graham, J. J. Berry, A. Kahn, D. C. Olson, Energy Environ. Sci. 8 (2015) 592-601.
[24] V. Gavryushin, G. Raciukaitis, D. Juodzbalis, A. Kazlauskas, V. Kubertavicius, J. Cryst. Growth 138 (1994) 924-933.
[25] S. Trost, K. Zilberberg, A. Behrendt, A. Polywka, P. Görrn, P. Reckers, J. Maibach, T. Mayer, T. Riedl, Adv. Energy Mater. 3 (2013) 1437-1444.
[26] M. Prosa, M. Tessarolo, M. Bolognesi, O. Margeat, D. Gedefaw, M. Gaceur, C. Videlot Ackermann, M. R. Andersson, M. Muccini, M. Seri, J. Ackermann, ACS Appl. Mater. Interfaces 2016, 8, 1635-1643.
[27] S. Wilken, J. Parisi, H. Borchert, J. Phys. Chem. C 118 (2014) 19672-19682.
[28] M. R. Lilliedal, A. J. Medford, M. V. Madsen, K. Norrman, F. C. Krebs, Sol. Energy Mater. Sol. Cells 94 (2010) 2018-2031.
[29] A. J. Morfa, B. I. MacDonald, J. Subbiah, J. J. Jasieniak, Sol. Ener. Mater. Sol. Cells 124 (2014) 211-216.
[30] S. Wilken, J. Parisi, H. Borchert, J. Phys. Chem. C 118 (2014) 19672-19682.
[31] Q. Bao, X. Liu, Y. Xia, F. Gao, L.-D. Kauffmann, O. Margeat, J. Ackermann, M. Fahlman, J. Mater. Chem. A 2 (2014) 17676-17682.
[32] H.-L. Yip, S. K. Hau, N. S. Baek, H. Ma, A. K.-Y. Jen, Adv. Mater. 20 (2008) 2376-2382.
[33] Y. E. Ha, M. Y. Jo, J. Park, Y.-C. Kang, S. I. Yoo, J. H. Kim, J. Phys. Chem. C 11(2013) 2646-2652.
[34] Y.-S. Cheng, S.-H. Liao, Y.-L. Li, S.-A. Chen, ACS Appl. Mater. Interfaces 5 (2013) 6665-6671.
[35] J. J. Intemann, K. Yao, Y.-X. Li, H.-L. Yip, Y. X. Xu, P.-W. Liang, C.-C. Chueh, F.-Z. Ding, X. Yang, X. Li, Y. Chen, A. K.-Y. Jen, Adv. Funct. Mater. 24 (2013) 1465-1473.
[36] I. Lange, S. Reiter, M. Pätzel, A. Zykov, A. Nefedov, J. Hildebrandt, S. Hecht, S. Kowarik, C. Wöll, G. Heimel, D. Neher, Adv. Funct. Mater. 24 (2014) 7014-7024.
[37] S. Bai, Y. Jin, X. Liang, Z. Ye, Z. Wu, B. Sun, Z. Ma, Z. Tang, J. Wang, U. Würfel, F. Gao, F. Zhang, Adv. Energy Mater. 5 (2015) 1401606.
[38] S. Shao, K. Zheng, T. Pullerits, F. Zhang, ACS Appl. Mater. Interfaces 5 (2013) 380-385.
[39] S. B. Jo, J. H. Lee, M. Sim, M. Kim, J. H. Park, Y. S. Choi, Y. Kim, S.-G. Ihn, K. Cho, Adv. Energy Mater. 1 (2011) 690-698.
[40] T. Hu, F. Li, K. Yuan, Y. Chen, ACS Appl. Mater. Interfaces 5 (2013) 5763-5770.
[41] X. Liu,X. Li, Y. Li,C. Song,L. Zhu,W.Zhang, H.-Q.Wang, J. Fang,Adv. Mater. 28(2016) 7405-7412.
[42] T. Stubhan, I. Litzov, N. Li, M. Salinas, M. Steidl, G. Sauer, K. Forberich, G. J. Matt, M. Halik, C. J. Brabec, J. Mater. Chem. A 1 (2013) 6004-6009.
[43] A. Puetz, T. Stubhan, M. Reinhard, O. Loesch, E. Hammarberg, S. Wolf, C. Feldmann, H. Kalt, A. Colsmann, U. Lemmer, Sol. Energy Mater. Sol. Cells 95 (2011) 579-585.

[44] A. Savva, S. A. Choulis, Appl. Phys. Lett. 102 (2013) 233301.

[45] H. Woo Choi, K.-S. Lee, N. David Theodore, T. L. Alford, Sol. Energy Mater. Sol. Cells 117 (2013) 273-278.

[46] K. P. Musselman, S. Albert-Seifried, R. L. Z. Hoye, A. Sadhanala, D. Muñoz-Rojas, J. L. MacManus-Driscoll, R. H. Friend, Adv. Funct. Mater. 24 (2014) 3562-3570.

[47] J. Adams, G. D. Spyropoulos, M. Salvador, N. Li, S. Strohm, L. Lucera, S. Langner, F. Machui, H. Zhang, T. Ameri, M. M. Voigt, F. C. Krebs, C. J. Brabec, Energy Environ. Sci. 8, (2015) 169-176.

[48] N. K Elumalai, C. Vijila, R. Jose, A. Uddin, S. Ramakrishna, Mater. Renew. Sustain. Energy 4:11 (2015) 1-25.

[49] C. G. Van de Walle, Phys. Rev. Lett. 85 (2000) 1012-1015.

[50] C. G. Van de Walle, J. Neugebauer, Nature 423 (2003) 626-628.

[51] A. Janotti, C. G. Van de Walle, Nat. Mater. 6 (2007) 44-47.

[52] V. Papamakarios, E. Polydorou, A. Soultati, N. Droseros, D. Tsikritzis, A. M. Douvas, L. Palilis, M. Fakis, S. Kennou, P. Argitis, M. Vasilopoulou, ACS Appl. Mater. Interfaces 8 (2016) 1194-1205.

[53] H. L. Gao, X. W. Zhang, J. H. Meng, Z. G. Yin, L. Q. Zhang, J. L. Wu, X. Liu, J. Mater. Chem. 3 (2015) 3719-3725.

[54] B.-Y. Oh, M.-C. Jeong, D.-S. Kim, W. Lee, J.-M. Myoung, J. Cryst. Growth 281 (2005) 475-480.

[55] Z. Kam, X. Wang, J. Zhang, J. Wu, ACS Appl. Mater. Interfaces 7 (2015) 1608-1615.

[56] Q. Liu, P. Mantilla-Perez, M. Montes Bajo, P. Romero-Gomez, J. Martorell, ACS Appl. Mater. Interfaces 8 (2016) 28750-28756.

[57] J. Reinhardt, M. Grein, C. Buhler, M. Schubert, U. Wurfel, Adv. Energy Mater. 5 (2014)1400081.

[58] M. Vasilopoulou, Nanoscale 6 (2014) 13726-13739.

[59] S. Trost, T. Becker, A. Polywka, P. Görrn, M. F. Oszajca, N. A. Luechinger, D. Rogalla, M. Weidner, P. Reckers, T. Mayer, T. Riedl, Adv. Energy Mater. 6 (2016)1600347.

[60] E. Polydorou, A. Soultati, M. Vasilopoulou, J. Mater. Chem. C. 4 (2016) 691-703.

[61] K. Ellmer, Nature Photonics 6 (2012) 809–817.

[62] L.-Y. Chen, W.-H. Chen, J.-J. Wang, F. Chau-Nan Hong, Appl. Phys. Lett. 85 (2004) 5628-5631.

[63] M. Willander, O. Nur, J. R. Sadaf, M. I. Qadir, S. Zaman, A. Zainelabdin, N. Bano, I. Hussain, Materials 3 (2010) 2643-2667.

[64] V. P. Singh, C. Rath, RSC Adv. 5 (2015) 44390-44397.

[65] E. M. Bachari, G. Baud, S. Ben Amor, Thin Solid Films 348 (1999) 165-172.

[66] M. G. Wardle, J. P. Goss, P. R. Briddon, Phys. Rev. B: Condens. Matter Mater. Phys. 72 (2005) 155108.

[67] B. R. Strohmeier, D. M. Hercules, J. Catal. 86 (1984) 266-279.

[68] O. Lupan, T. Pauporté, L. Chow, B. Viana, F. Pellé, L.K. Ono, B. Roldan Cuenya, H. Heinrich, Appl. Surf. Sci. 256 (2010) 1895-1907.

[69] M. Chen, X. Wang, Y. H Yu, Z. L Pei, X. D Bai, C. Sun, R. F Huang, L. S Wen, Appl. Surf. Sci. 158 (2000) 134-140.

[70] B. K. Stuhl, M. T. Hummon, M. Yeo, G. Quéméner, J. L. Bohn, J. Ye, Nature 492 (2012) 396-401.

[71] P. Cheng, Y. Li, X. Zhan, Energy Environ. Sci. 7 (2014) 2005-2011.

[72] M. Vasilopoulou, L. C. Palilis, D. G. Georgiadou, S. Kennou, I. Kostis, D. Davazoglou, P. Argitis, P. Appl. Phys. Lett. 100 (2012) 013311.

[73] Z. Xu, L.-M. Chen, M.-H. Chen, G. Li, Y. Yang, Appl. Phys. Lett. 95 (2009) 013301.

[74] Q. Bao, X. Liu, Yuxin Xia, Feng Gao, L.-D. Kauffmann, O. Margeat, J. Ackermannc, M. Fahlmana, Mater. Chem. A 2 (2014) 17676

[75] Y.-J. Siao, P.-L. Liu, Y.-T. Wu, Appl. Phys. Expr. 4 (2011) 125601.

[76] J. Briscoe, D. E. Gallardo, S. Hatch, V. Lesnyak, N. Gaponik, S. Dunn, J. Mater. Chem. 21 (2011) 2517-2523.

[77] I. Kostis, N. Vourdas, G. Papadimitropoulos, A. Douvas, M. Vasilopoulou, N. Boukos, D. Davazoglou, J. of Phys. Chem. C 117 (2013) 18013-18020.

[78] H. Li, L. K. Schirrar, J. Shim, H. Cheun, B. Kippelen, O. L. A. Monti, L.-L. Bredas, Chem. Mater. 2012, 24, 3044-3055.

[79] E. H. Kisi, M. M. Elcombe, Acta Crystallogr., Sect. C: Struct. Commun. 45 (1989) 1867-1870.